ACS APPLIED MATERIALS & INTERFACES

Research Article

www.acsami.org

Two-Dimensional $CaIn_2S_4$/g-C_3N_4 Heterojunction Nanocomposite with Enhanced Visible-Light Photocatalytic Activities: Interfacial Engineering and Mechanism Insight

Deli Jiang, Jie Li, Chaosheng Xing, Zhengyuan Zhang, Suci Meng, and Min Chen*

School of Chemistry and Chemical Engineering, Jiangsu University, Zhenjiang, Jiangsu 212013, China

Ⓢ *Supporting Information*

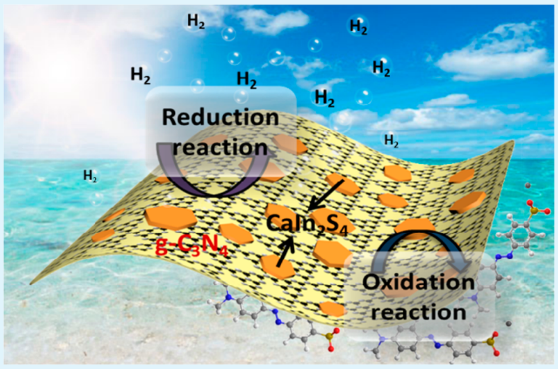

ABSTRACT: Design and exploitation of efficient visible light photocatalytic systems for water splitting and degradation of organic dyes are of huge interest in the fields of energy conversion and environmental protection. Herein, two-dimensional $CaIn_2S_4$/g-C_3N_4 heterojunction nanocomposites with intimate interfacial contact have been synthesized by a facile two-step method. Compared with pristine g-C_3N_4 and $CaIn_2S_4$, the $CaIn_2S_4$/g-C_3N_4 heterojunction nanocomposites exhibited significantly enhanced H_2 evolution and photocatalytic degradation of methyl orange (MO) activities under visible light irradiation. The optimal $CaIn_2S_4$/g-C_3N_4 nanocomposite shows a H_2 evolution rate of 102 μmol g^{-1} h^{-1}, which is more than 3 times that of pristine $CaIn_2S_4$. The mechanisms for improving the photocatalytic performance of the $CaIn_2S_4$/g-C_3N_4 nanocomposites were proposed by using the photoluminescence measurement and electrochemical analyses. It was demonstrated that the enhanced photocatalytic performance of $CaIn_2S_4$/g-C_3N_4 heterojunction nanocomposites mainly stems from the enhanced charge separation efficiency. In addition, a plausible mechanism for the degradation of MO dye over $CaIn_2S_4$/g-C_3N_4 nanocomposites is also elucidated using active species scavenger's studies.

KEYWORDS: *g-C_3N_4, $CaIn_2S_4$, two-dimensional interface, photocatalytic activity, mechanism*

1. INTRODUCTION

Since the photocatalytic system of water splitting on TiO_2 electrodes was discovered by Fujishima and Honda in 1972,[1] photocatalytic H_2 evolution and degradation of organic pollutants using semiconductors has become the most attractive and sustainable strategy to solve the global energy crisis and environmental pollution.[2−5] In order to make full use of sunlight, especially the visible-light which accounts for more than 40% of the incoming solar energy, extensive efforts have been undertaken to develop visible-light driven photocatalysts and composite photocatalytic systems. Up to now, a large number of visible-light responsive photocatalytic materials have been developed.[6−10] However, the insufficient stability and low efficiency still render the overall process impractical. Thus, exploitation of visible-light-driven photocatalysts with high efficiency is still a great challenge.

Graphitic carbon nitride (g-C_3N_4), especially the two-dimensional g-C_3N_4 nanosheets, due to their large surface area, narrow band gap, fast charge transfer rate, and excellent stability, has recently been regarded as a promising visible-light-responsive candidate for water splitting and organic degradation.[11−14] However, g-C_3N_4 materials that are low efficiency caused by the fast charge recombination for practical use of g-C_3N_4 have not yet been realized.[15,16] To overcome the inherent problems and improve the photocatalytic activity of g-C_3N_4, various methods have been developed, including morphology control, doping and coupling with metal, nonmetal, carbon dots, and graphene.[17−20] Besides these, cooperating with other semiconductor photocatalysts to form the heterojunction is an effective way to promote the separation of the photogenerated electron−hole pairs.[21,22] Li et al. constructed efficient $BiVO_4$/g-C_3N_4 heterojunction nanocomposites with enhanced photocatalytic activity for degradation of MO, and they considered that the suitable energy band alignments could benefit the charge separation.[23] Fu et al. synthesized the CdS/g-C_3N_4 composite by an "in situ" precipitation-deposition method. The as-prepared composite showed exceptional photocatalytic activity owing to the existence of organic−inorganic heterojunctions.[24] Our group has recently developed a p-n heterojunction photocatalyst which was constructed by BiOI and g-C_3N_4. The enhanced visible-light photocatalytic activity could be attributed to the strong absorption in visible region and high charge separation efficiency which was ascribed to the heterojunction formed between BiOI and g-C_3N_4.[25] However, the two-dimensional g-C_3N_4-based heterojunctions with enhanced photocatalytic activities of both water splitting and

Received: June 10, 2015
Accepted: August 18, 2015
Published: August 18, 2015

ACS Publications © 2015 American Chemical Society

DOI: 10.1021/acsami.5b05118
ACS Appl. Mater. Interfaces 2015, 7, 19234−19242

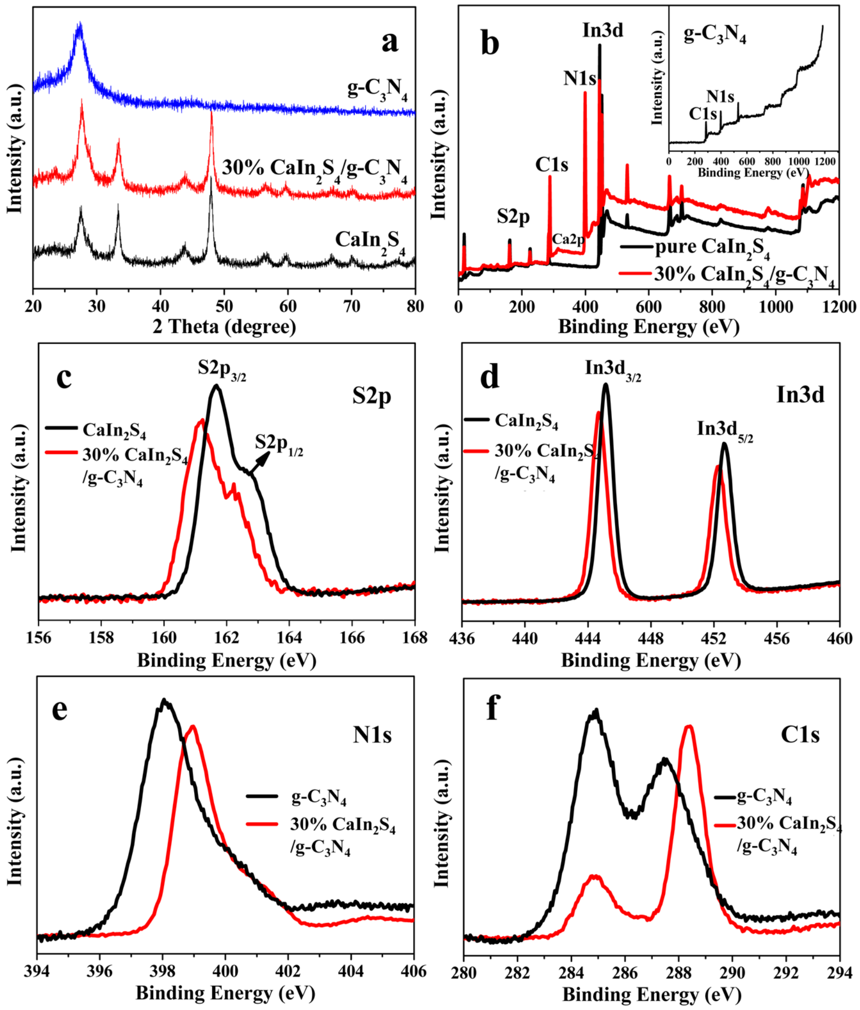

Figure 1. (a) XRD patterns of g-C_3N_4, 30% $CaIn_2S_4$/g-C_3N_4, and $CaIn_2S_4$ heterojunction nanocomposite, (b) survey XPS spectra of g-C_3N_4 (insert), 30% $CaIn_2S_4$/g-C_3N_4 and $CaIn_2S_4$ heterojunction nanocomposite, (c, d) high resolution spectra of S and In for $CaIn_2S_4$ and 30% $CaIn_2S_4$/g-C_3N_4 heterojunction nanocomposite, (e, f) high resolution spectra of N and C for g-C_3N_4 and 30% $CaIn_2S_4$/g-C_3N_4 heterojunction nanocomposite.

photocatalytic degradation of organic dyes have been rarely reported.

In this work, as a typical ternary metal sulfide, cubic $CaIn_2S_4$ material has been employed to construct a two-dimensional heterojunction photocatalyst with g-C_3N_4 due to its suitable band gap, good activity, and excellent stability.[26,27] The formed two-dimensional heterostructure of the nanocomposite photocatalyst could not only enhance the interfacial contact area between $CaIn_2S_4$ and g-C_3N_4 but also facilitate separation of charge carriers. As such, the $CaIn_2S_4$/g-C_3N_4 heterojunction nanocomposites exhibited enhanced H_2 evolution and photocatalytic degradation of MO activities under visible-light irradiation in comparison to pristine g-C_3N_4 and $CaIn_2S_4$. The possible relative electron transfer models and photocatalytic mechanisms for cocatalyst induced H_2 production and dye degradation mechanisms have been investigated. This work may provide useful insights to design and prepare two-dimensional heterojunction photocatalysts with enhanced photocatalytic activity.

2. EXPERIMENTAL SECTION

2.1. Preparation of Photocatalysts. g-C_3N_4 nanosheets were prepared according to the previously reported method.[25] In a typical procedure for the synthesis of the $CaIn_2S_4$/g-C_3N_4 heterojunction nanocomposite, 0.2 g of g-C_3N_4 powders and 0.0354 g of $Ca(NO_3)_2\cdot 4H_2O$ were dissolved in 80 mL of deionized water; after ultrasonication for 40 min, 0.1146 g of $In(NO_3)_3$ and 0.09 g of C_2H_5NS were added into the solution under stirring. After having been stirring for 1 h, the obtained mixture was transferred to a 50 mL Teflon-lined stainless steel autoclave, which was heated to 120 °C and maintained for 24 h. After cooling, the as-prepared product (denoted as 30% $CaIn_2S_4$/g-C_3N_4) was collected by centrifugation, washed with distilled water and absolute ethanol, and dried at 60 °C overnight. By changing the addition amount of $Ca(NO_3)_2\cdot 4H_2O$, $In(NO_3)_3$, and C_2H_5NS, 20% $CaIn_2S_4$/g-C_3N_4, 40% $CaIn_2S_4$/g-C_3N_4, and 50% $CaIn_2S_4$/g-C_3N_4 nanocomposites were obtained.

2.2. Characterization. The phase purity and crystal structure of the obtained photocatalysts were tested by X-ray diffraction (XRD, Bruker D8 Advance X-ray diffractometer) with Cu−Kα radiation (λ = 1.5406 Å). Infrared spectra were obtained on KBr pellets on a Nicolet NEXUS470 FTIR in the range of 4000−500 cm^{-1}. Transmission electron microscopy (TEM) and scanning transmission electron microscopy (STEM) were recorded on a Tecnai G2 F30 S-TWIN (Philips) operating at 300 kV. Surface analysis of the photocatalysts was examined by X-ray photoelectron spectroscopy (XPS) using a ESCA PHI500 spectrometer. The surface areas of the photocatalysts were measured by a TriStar II 3020-BET/BJH Surface Area. UV−vis diffuse reflectance spectra (DRS) were performed on a Shimadzu UV-2401 spectrophotometer equipped with a spherical diffuse reflectance

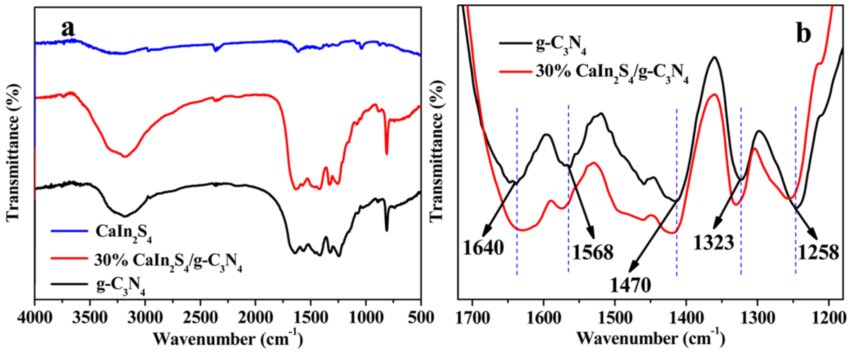

Figure 2. FT-IR spectra of g-C_3N_4, 30% $CaIn_2S_4$/g-C_3N_4, and $CaIn_2S_4$ heterojunction nanocomposites (a) and the magnified curves in the range of 1180 cm^{-3} to 1720 cm^{-3} in FT-IR spectra (b).

accessory. The photoluminescence (PL) spectra of the photocatalyst were obtained by a Varian Cary Eclipse spectrometer with an excitation wavelength of 325 nm. The electron spin resonance (ESR) signals of spin-trapped radicals were conducted on a Bruker model ESR JES-FA200 spectrometer using spin-trap reagent DMPO in water and methanol, respectively.

2.3. Photocatalytic Hydrogen Evolution. Prior to H_2 evolution, 1.0 wt % Pt-dispersed photocatalysts were fabricated by an in situ photodeposition method using hexachloroplatinic acid (H_2PtCl_6) as a precursor under 300 W xenon lamp irradiation for 1 h. The photocatalytic hydrogen evolution experiments were performed in a 100 mL Pyrex flask connected to a closed gas circulation and evacuation system. Four low power UV-LEDs (3 W, 420 nm) (Shenzhen LAMPLIC Science Co. Ltd. China), employed as light sources to induce the photocatalytic reaction, were positioned ca. 1 cm away from the flask in four different directions. The focused intensity and areas on the flask for each UV-LED was ca. 80.0 mW•cm^{-2} and 1 cm^2, respectively. Typically, 0.05 g of photocatalyst was dispersed by a magnetic stirrer in 80 mL of aqueous solution containing 0.5 M Na_2S and 0.5 M Na_2SO_3. Prior to irradiation, the suspension of the photocatalyst was dispersed by an ultrasonic bath for 5 min and then bubbled with nitrogen for 20 min to completely remove the dissolved oxygen and create an anaerobic condition. A 0.4 mL gas was intermittently sampled through the septum, and the amount of H_2 was determined by gas chromatography (GC-14C, Shimadzu, Japan, TCD, with nitrogen as a carrier gas and 5 Å molecular sieve column).

2.4. Photocatalytic Degradation of MO. The photocatalytic activities of the g-C_3N_4/$ZnIn_2S_4$ photocatalysts were tested in the degradation reaction of MO aqueous solution (10 mg/L) under irradiation of a 500 W tungsten light lamp. For a typical photocatalytic degradation experiment, 50 mg of photocatalyst powder was added into 100 mL of the above MO solution in a quartz tube. Prior to irradiation, the suspensions were magnetically stirred in dark for 30 min to ensure the establishment of an adsorption/desorption equilibrium. The above suspensions were kept under constant air-equilibrated conditions before and during the irradiation. At given time intervals, about 4 mL of aliquots was sampled and centrifuged to remove the particles. The filtrates were analyzed by a Shimadzu UV-2450 spectrophotometer, and the characteristic absorption peak of MO at 462 nm was used to determine the extent of its degradation.

2.5. Photoelectrochemical Measurement. To investigate the photoelectrochemical properties of as-prepared photocatalysts, the modified electrodes were prepared as follows: 4 mg of the as-prepared photocatalyst (g-C_3N_4, $CaIn_2S_4$, and 30% $CaIn_2S_4$/g-C_3N_4, respectively) was suspended in 1 mL of ethanol and 20 μL of 5 wt % Nafion solution to produce a slurry, which 30 μL of the resulting colloidal dispersion then getting dropped onto a piece of FTO slice with a fixed area of 1 cm^2. All the photoelectrochemical measurements were measured on an electrochemical analyzer in a standard three-electrode system using the prepared samples as the working electrode, a Pt wire as the counter electrode, and Ag/AgCl as a reference electrode. A 500 W Xe arc lamp served as a light source. The photocurrent was performed in 0.2 M Na_2SO_4 aqueous solution.

3. RESULTS AND DISCUSSION

The crystal structure and phase composition of g-C_3N_4, 30% $CaIn_2S_4$/g-C_3N_4, and $CaIn_2S_4$ were characterized by XRD. As shown in Figure 1a, the XRD pattern of g-C_3N_4 exhibits two distinct diffraction peaks at 13.2° and 27.5°, corresponding to (002) and (100) diffraction planes of graphitic carbon nitride, respectively. Pure and well-crystallized cubic phase $CaIn_2S_4$ was confirmed by XRD pattern of the $CaIn_2S_4$ sample, of which all the diffraction peaks can be indexed to cubic phase $CaIn_2S_4$ (JCPDS#16-0341). After $CaIn_2S_4$ composing with g-C_3N_4, due to the close peak position of $CaIn_2S_4$ and g-C_3N_4 at 27.5°, the XRD pattern of the heterojunction nanocomposite is similar as the pure $CaIn_2S_4$. However, when tuning the proportion of $CaIn_2S_4$, the peak intensities of XRD patterns change greatly (Figure S1), which reveals the existence of both $CaIn_2S_4$ and g-C_3N_4.

The chemical states of different elements of g-C_3N_4, the 30% $CaIn_2S_4$/g-C_3N_4 heterojunction nanocomposite, and $CaIn_2S_4$ were investigated by XPS. The survey scans spectrum indicates the presence of Ca, In, S in $CaIn_2S_4$, Ca, In, S, C, and N in the 30% $CaIn_2S_4$/g-C_3N_4 nanocomposite, and C, N in g-C_3N_4, respectively (Figure 1b). High resolution S 2p spectra of the 30% $CaIn_2S_4$/g-C_3N_4 shows two peaks at 161.2 and 162.3 eV, corresponding to the S $2p_{3/2}$ and S $2p_{1/2}$, respectively (Figure 1c).[28,29] As shown in Figure 1d, the peaks at the binding energies of 444.6 and 454.2 eV are attributed to the In $3d_{5/2}$ and In $3d_{3/2}$, respectively.[28,29] The N 1s peak for the 30% $CaIn_2S_4$/g-C_3N_4 can be deconvoluted into three peaks with binding energy at 398.9, 399.8, and 401.0 eV (Figure 1e and Figure S2). The peak at 398.9 eV is assigned to sp^2-hybridized N (C=N−C), and the other two peaks at 399.8 and 401.0 eV are ascribed to tertiary N ($N-(C)_3$) and amino functional groups having a H atom (C−N−H).[30,31] Meanwhile, the C 1s was also examined (Figure 1f). The binding energies of 284.9 and 288.4 eV of C 1s for the 30% $CaIn_2S_4$/g-C_3N_4 can be assigned to adventitious carbon on the surface of the sample and C−N−C coordination.[32] Thus, these results could confirm the existence of graphite-like carbon nitride in the composite. It is worth noting that both the peaks of S 2p and In 3d for the 30% $CaIn_2S_4$/g-C_3N_4 shift toward lower binding energies, while N 1s and C 1s (mainly the peak of C−N−C coordination) shift toward higher binding energies relative to $CaIn_2S_4$ and g-C_3N_4. These shifts might result from a partial electron transfer from the electron-rich structure of g-C_3N_4 to $CaIn_2S_4$,[33] and this would increase the electron density of $CaIn_2S_4$, leading to reduction of the binding energies of S 2p and In 3d. On the other hand, the electron density of g-C_3N_4 could be decreased,

DOI: 10.1021/acsami.5b05118
ACS Appl. Mater. Interfaces 2015, 7, 19234−19242

leading to the enhancement of binding energies of N 1s and C 1s. These results indicate a strong electronic interaction between $CaIn_2S_4$ and $g\text{-}C_3N_4$,[34] and this is beneficial to the transfer of photoinduced charges during the photocatalytic process.

The composition and structure of the $CaIn_2S_4/g\text{-}C_3N_4$ heterojunction nanocomposites were further confirmed by FT-IR spectra. As shown in Figure 2a, $g\text{-}C_3N_4$ is indicated by several characteristic absorptions at wavenumbers of 1640, 1568, 1407, 1323, and 1258 cm^{-3}. For $g\text{-}C_3N_4$, the peak at 1640 cm^{-3} is attributable to C=N stretching vibration. Additionally, the peaks at 1568, 1407, 1323, and 1258 cm^{-3} could correspond to aromatic C−N stretching.[32,35] When the heterojunction formed between $CaIn_2S_4$ and $g\text{-}C_3N_4$, it can be concerned clearly a red shift of the peak at 1640 cm^{-3} and a blue shift of the peaks at 1407, 1323, and 1258 cm^{-3} from the FT-IR curve of the 30% $CaIn_2S_4/g\text{-}C_3N_4$ heterojunction nanocomposite. We proposed a possible explanation to this phenomenon. When the heterojunction was formed, due to a partial electron transfer from $g\text{-}C_3N_4$ to $CaIn_2S_4$, the dispersibility of electron of $g\text{-}C_3N_4$ could be enhanced, and then the conjugated effect of $g\text{-}C_3N_4$ will be improved. As a result, the vibration intensity of C=N will be reduced, and the peak which generated by C=N stretching vibration will shift to lower wavenumber. On the other hand, the vibration intensity of C−N will be enhanced, and the peak which generated by C−N stretching vibration will shift to higher wavenumber. The IR spectra for 20%, 40%, and 50% $CaIn_2S_4/g\text{-}C_3N_4$ heterojunction nanocomposites show the similar results as the 30% $CaIn_2S_4/g\text{-}C_3N_4$ (Figure S3). On the basis of the above XPS as well as FT-IR results, it can be assumed that there is strong interfacial interaction between the $g\text{-}C_3N_4$ and $CaIn_2S_4$, which could facilitate the transfer of photoinduced charge and consequently improve the photocatalytic activity of $CaIn_2S_4/g\text{-}C_3N_4$ nanocomposites.

In order to confirm the detail morphology of the $CaIn_2S_4/g\text{-}C_3N_4$ heterojunction nanocomposites, TEM and STEM-EDS mapping have been introduced. As shown in Figure 3a, the $g\text{-}C_3N_4$ exhibits thin and irregular nanosheet structure with wrinkles, in agreement with the typical structural characteristic of graphite-like carbon nitride. In Figure 3b, the TEM image shows the as-prepared $CaIn_2S_4$ is an irregular nanoplate with a diameter of around 20 nm. Figure 3c and 3d show the typical structure of the 30% $CaIn_2S_4/g\text{-}C_3N_4$ nanocomposite. The $CaIn_2S_4$ nanoplates anchor dispersedly across the $g\text{-}C_3N_4$ nanosheets, which form a two-dimensional heterostructure with intimate interfacial contact. It is worth mentioning that the two-dimentional structure could effectively improve the specific surface area (Figure S4), which is beneficial to the phtocatalytic activity by providing abundant reactive sites to trap charge carriers and adsorb reactant species.[36,37] The selected region marked by the red lines in Figure 3c is magnified to examine the detailed structure of the 30% $CaIn_2S_4/g\text{-}C_3N_4$ nanocomposite (Figure 3d). As shown in Figure 3e, the clear lattice fringes with a *d*-spacing of 0.278 nm, corresponding to the (400) planes of cubic phase $CaIn_2S_4$, indicating the nanoplates are $CaIn_2S_4$ with the two-dimensional structure. The morphology of the 30% $CaIn_2S_4/g\text{-}C_3N_4$ nanocomposite was further confirmed by the HAADF-STEM image (Figure 3f). The elemental mappings (Figure 3g) reveal that Ca, In, S, C, and N elements coexistently distributed in the 30% $CaIn_2S_4/g\text{-}C_3N_4$ nanocomposite, and the $CaIn_2S_4$ dispersed on the surface of $g\text{-}C_3N_4$ also can be confirmed by the signals intensity of different elements. With increasing the content of $CaIn_2S_4$, the nanoplates in the two-dimensional heterojunction nanocomposites increased correspondingly, which is shown in Figure S5.

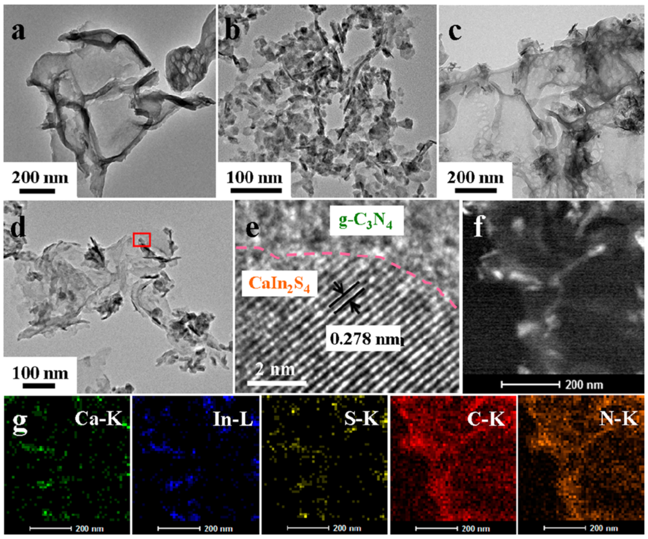

Figure 3. TEM images of (a) $g\text{-}C_3N_4$, (b) $CaIn_2S_4$, (c, d) the 30% $CaIn_2S_4/g\text{-}C_3N_4$ heterojunction nanocomposite, the HRTEM image of the 30% $CaIn_2S_4/g\text{-}C_3N_4$ heterojunction nanocomposite (e), HAADF-STEM-EDS mapping (f) and the spatially resolved Ca, In, S, C, and N elements of the 30% $CaIn_2S_4/g\text{-}C_3N_4$ heterojunction nanocomposite (g).

The optical properties of the $CaIn_2S_4/g\text{-}C_3N_4$ heterojunction nanocomposites were evaluated by UV−vis diffusive absorption spectroscopy. Figure 4a shows the ultraviolet−visible diffusive absorption spectra of $CaIn_2S_4$, $g\text{-}C_3N_4$ and $CaIn_2S_4/g\text{-}C_3N_4$ heterojunction nanocomposites with different contents of $CaIn_2S_4$. It can be seen that $CaIn_2S_4$ and $g\text{-}C_3N_4$ can absorb visible-light with wavelengths about 618 and 437 nm, and the band gaps which estimated from the UV−vis spectra are around 2.01 and 2.83 eV (by the equation: $\lambda = 1240/Eg$), respectively, which is in good agreement with the previous results.[11,26] The absorption spectra of $CaIn_2S_4/g\text{-}C_3N_4$ heterojunction nanocomposites exhibit the combination of both spectra which contributes from $CaIn_2S_4$ and $g\text{-}C_3N_4$. Besides, the absorption peak slight red-shifts with increasing intensities when the content of $CaIn_2S_4$ is increased from 20% to 50%. As a result, this enhanced visible light adsorption in the $CaIn_2S_4/g\text{-}C_3N_4$ could generate more photoinduced charge carriers, which would contribute to the enhanced photocatalystic activity. The valence bands (VB) of both $CaIn_2S_4$ and $g\text{-}C_3N_4$ are measured by XPS valence spectra, as shown in Figure 4b. It could be clearly observed that the position of the VB edge of $CaIn_2S_4$ and $g\text{-}C_3N_4$ are located at 1.03 and 1.71 eV, respectively, which are consistent with the previous reports.[26,38] Combined with the calculated band gaps, the conduction band (CB) edge of $CaIn_2S_4$ and $g\text{-}C_3N_4$ are estimated at −0.98 eV and −1.12 eV, respectively.

Figure 5a shows the photocatalytic H_2 production activity of $g\text{-}C_3N_4$, $CaIn_2S_4$, and $CaIn_2S_4/g\text{-}C_3N_4$ heterojunction nanocomposites with different contents of $CaIn_2S_4$ from an aqueous solution containing 0.5 M Na_2S and 0.5 M Na_2SO_3 under UV light irradiation (triggered by 12 W UV-LEDs light). It can be seen that the H_2 evolution is negligible over the pristine $g\text{-}C_3N_4$, which is consistent with the previous report,[39,40] and the

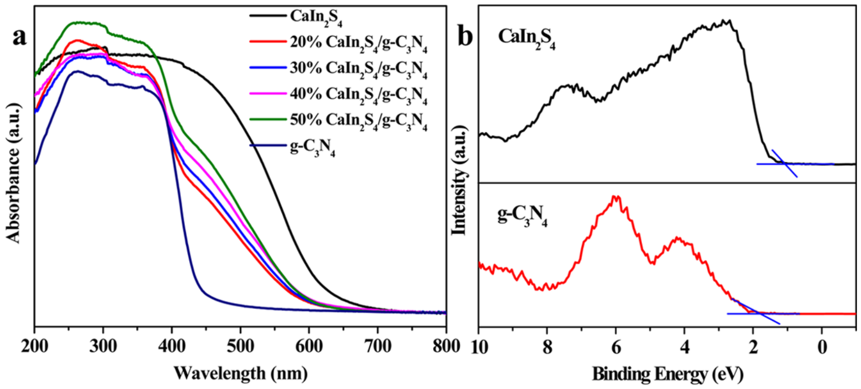

Figure 4. (a) Ultraviolet−visible diffusive absorption spectra the photocatalysts and (b) valence band spectra of $CaIn_2S_4$ and $g\text{-}C_3N_4$.

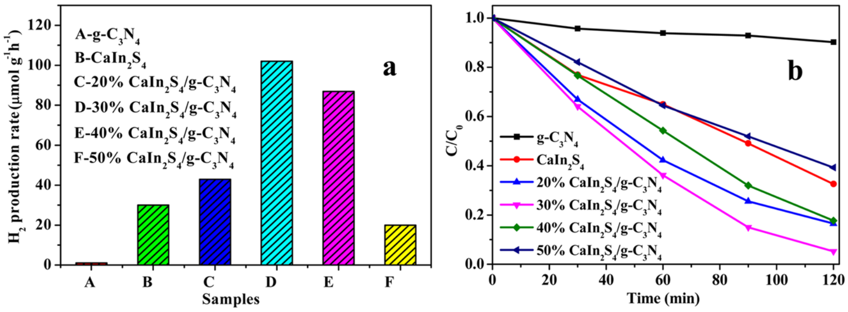

Figure 5. (a) Comparison of the photocatalytic H_2 production activity under visible light irradiation (triggered by 12 W UV-LEDs light) and (b) photocatalytic degradation efficiency under visible light irradiation (triggered by 500 W tungsten light lamp) over $g\text{-}C_3N_4$, $CaIn_2S_4$, and $CaIn_2S_4/g\text{-}C_3N_4$ nanocomposites with different contents of $CaIn_2S_4$.

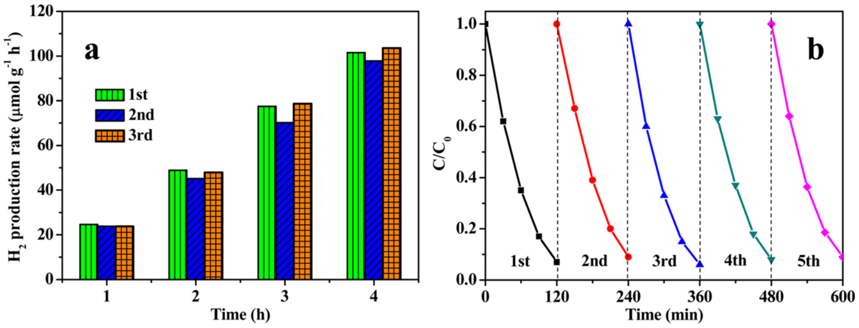

Figure 6. (a) Stability study of photocatalytic H_2 production activity and (b) photocatalytic degradation efficiency over the 30% $CaIn_2S_4/g\text{-}C_3N_4$ heterojunction nanocomposite.

rate of H_2 evolution over the pristine $CaIn_2S_4$ is 30 μmol g^{-1} h^{-1}. When forming the $CaIn_2S_4/g\text{-}C_3N_4$ heterojunction, the photocatalytic H_2 production activity was remarkably enhanced (except the 50% $CaIn_2S_4/g\text{-}C_3N_4$ sample). In particular, the 30% $CaIn_2S_4/g\text{-}C_3N_4$ heterojunction nanocomposite shows the maximum H_2 evolution rate of 102 μmol g^{-1} h^{-1}, which is more than three times that of pristine $CaIn_2S_4$ with a large BET surface area (Figure S4). However, the excess $CaIn_2S_4$ (50 wt % in the composite) decreased the H_2 evolution rate. This phenomenon can be explained as follows: (1) at a very high content of $CaIn_2S_4$, the $CaIn_2S_4$ will be more apt to self-aggregation, the existence of $CaIn_2S_4/g\text{-}C_3N_4$ heterojunction will be decreased, which leads to a lower H_2 evolution rate than other heterojunction photocatalysts; (2) owing to the same dosage used in the photocatalytic test of different photocatalysts, the actual amount of $CaIn_2S_4$ in the 50% $CaIn_2S_4/g\text{-}C_3N_4$ heterojunction nanocomposite is less than the pure $CaIn_2S_4$, resulting in the lower H_2 evolution rate than pristine $CaIn_2S_4$. Therefore, a suitable content of $CaIn_2S_4$ is crucial for optimizing the photocatalytic activity of $CaIn_2S_4/g\text{-}C_3N_4$ nanocomposites.

To further investigate the photocatalytic activity of the as-prepared $CaIn_2S_4/g\text{-}C_3N_4$ nanocomposites, photocatalytic degradation of MO under visible light irradiation has been carried out in this study. In general, the tendency of photocatalytic degradation efficiency is similar to the tendency of the H_2 production rate over the different photocatalysts. As shown in Figure 5b, the degradation rate of MO over the $g\text{-}C_3N_4$ and $CaIn_2S_4$ only reaches 10% and 65% under visible light irradiation for 120 min. In contrast, the $CaIn_2S_4/g\text{-}C_3N_4$ heterojunction nanocomposites exhibit significantly enhanced photocatalytic activity in the degradation of MO, except for the 50% $CaIn_2S_4/g\text{-}C_3N_4$ sample. The highest activity is obtained for the 30% $CaIn_2S_4/g\text{-}C_3N_4$ heterojunction nanocomposite, over which more than 90% of MO was degraded after 120 min. The 50% $CaIn_2S_4/g\text{-}C_3N_4$ heterojunction nanocomposite

DOI: 10.1021/acsami.5b05118
ACS Appl. Mater. Interfaces 2015, 7, 19234−19242

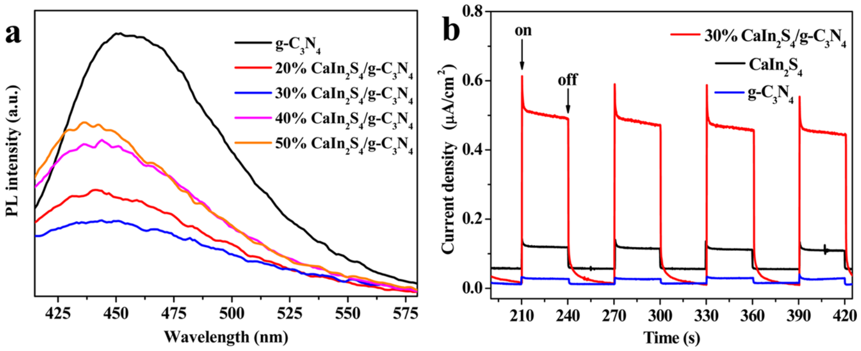

Figure 7. (a) Photoluminescence (PL) spectra of g-C_3N_4 and $CaIn_2S_4$/g-C_3N_4 heterojunction nanocomposites with different contents of $CaIn_2S_4$ and (b) transient photocurrent responses of the g-C_3N_4, $CaIn_2S_4$, and 30% $CaIn_2S_4$/g-C_3N_4 heterojunction nanocomposite.

exhibits the lowest photocatalytic activity among the heterojunction nanocomposites, and only ~60% of MO can be removed.

The catalyst lifetime is of great importance besides the photocatalytic performance. The photostability of $CaIn_2S_4$/g-C_3N_4 heterojunction nanocomposites were investigated by recycling the 30% $CaIn_2S_4$/g-C_3N_4 sample under the same conditions as the first test. As shown in Figure 6a and Figure 6b, after three and five recycles, both the H_2 evolution rate and the activity of photocatalytic degradation of MO did not show a significant decrease, and the phase of the photocatalyst used also has almost no change, as shown in Figure S6. These results indicate that the as-prepared $CaIn_2S_4$/g-C_3N_4 heterojunctions have relatively high stabilities during photocatalytic H_2 production and degradation of MO.

In order to investigate the photocatalytic mechanism, PL spectroscopy measurements to analyze the charge recombination for g-C_3N_4, $CaIn_2S_4$, and $CaIn_2S_4$/g-C_3N_4 heterojunction nanocomposites with different contents of $CaIn_2S_4$ were investigated. As shown in Figure 7a, the pure g-C_3N_4 exhibits a strong emission in the range of 430−500 nm, which corresponds to the band gap carrier recombination.[41,42] When the $CaIn_2S_4$ was added, the PL emission intensity decreases markedly, which suggests that the photoinduced charge could be efficiently separated when the heterojunction was formed between g-C_3N_4 and $CaIn_2S_4$, and this further confirmed the photocatalytic mechanism proposed. The 30% $CaIn_2S_4$/g-C_3N_4 shows the lowest PL emission intensity, consistent with the photocatalytic performance of this sample.

The improved carrier separation efficiency of the $CaIn_2S_4$/g-C_3N_4 nanocomposite was further confirmed by the transient photocurrent responses of g-C_3N_4, $CaIn_2S_4$, and 30% $CaIn_2S_4$/g-C_3N_4. Figure 7b shows a comparison of the photocurrent−time (*I*-*t*) curves for these samples with typical on−off cycles of intermittent visible light irradiation. Notably, the photocurrent value of 30% $CaIn_2S_4$/g-C_3N_4 is several times higher than pristine g-C_3N_4 and $CaIn_2S_4$, which can be ascribed to the existence of two-dimensional interfaces between $CaIn_2S_4$ and g-C_3N_4, where photogenerated electrons and holes could be efficiently separated in space and the photoinduced carrier recombination will be reduced. As a result, the 30% $CaIn_2S_4$/g-C_3N_4 sample shows an enhanced photocurrent. The improved transfer efficiency of charge carriers could lead to the enhanced photocatalytic activity of $CaIn_2S_4$/g-C_3N_4 nanocomposites.

To investigate the reaction mechanism in depth, the active species formed during the reaction process are identified by a hole and free radical trapping experiment over the 30% $CaIn_2S_4$/g-C_3N_4 sample. The *tert*-butanol (*t*-BuOH), ammonium oxalate (AO), and 1,4-benzoquinone (BQ) were used to detect the hydroxyl radical (•OH) scavenger, the hole (h^+) scavenger, and superoxide ($O_2^{\bullet -}$), respectively. As shown in Figure 8, the photocatalytic activity of 30% $CaIn_2S_4$/g-C_3N_4 decreases slightly by the addition of the hydroxyl radical but reduces greatly with the addition of hole scavengers and superoxide radical scavengers. Furthermore, a controlled experiment in a N_2 atmosphere indicates that the degradation ratio of MO is decreased, implying that the O_2 primarily acted as efficient electron traps, leading to the generation of $O_2^{\bullet -}$. These results clearly evidenced that photogenerated h^+ and $O_2^{\bullet -}$ are the main oxidative species for the degradation of MO in the photocatalytic system.

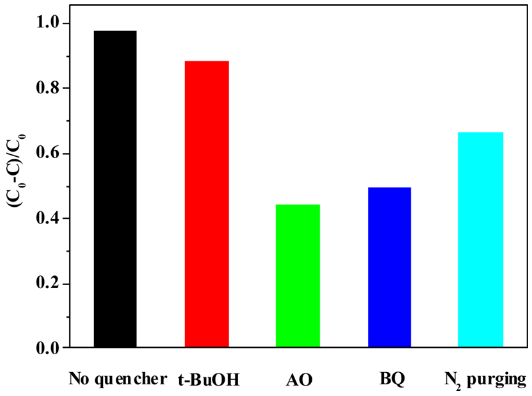

Figure 8. Controlled experiments of photocatalytic degradation of MO over the 30% $CaIn_2S_4$/g-C_3N_4 with the addition of different radical scavengers.

To further detect reactive oxygen species formed over 30% $CaIn_2S_4$/g-C_3N_4 during the degradation process, the electron spin resonance (ESR) spin-trap technique was used. As presented in Figure 9a, the ESR signals intensities of the 30% $CaIn_2S_4$/g-C_3N_4 sample under visible light irradiation is almost the same as in the dark case, suggesting that there is no •OH generated in this system and it was not the main reactive species. However, the characteristic peaks of DMPO−$O_2^{\bullet -}$ can be clearly detected in the methanol dispersion of 30% $CaIn_2S_4$/g-C_3N_4 under visible light irradiation (Figure 9b). Therefore, it is well recognized that $O_2^{\bullet -}$ can be produced and plays an important role in the degradation process of MO.

On the basis of the above results, an illustration of possible interface electron transfer behavior and the corresponding photocatalytic H_2 production mechanism were demonstrated

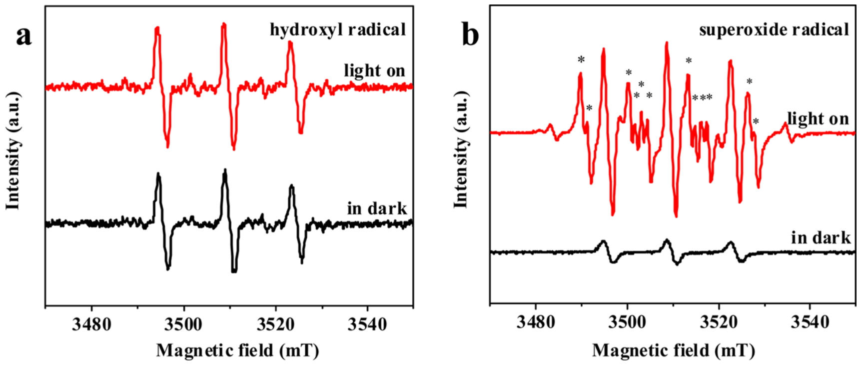

Figure 9. DMPO spin-trapping ESR spectra recorded with 30% $CaIn_2S_4/g\text{-}C_3N_4$ in (a) aqueous dispersion (for DMPO−•OH) and methanol dispersion (for DMPO−$O_2^{\bullet -}$) under visible light irradiation.

and shown in Figure 10a. Under visible light illumination, the photogenerated electrons and holes were excited from the VB and CB of $g\text{-}C_3N_4$ and then transfer to the VB and CB of $CaIn_2S_4$, respectively. Due to the high Fermi level of metallic noble metal Pt,[43] it can serve as a photoexcited electron acceptor, which could induce the photoexcited electrons fast transfer to the loaded Pt cocatalyst to generate H_2.[44−46] Our observation is similar to the result by Guo and co-workers, who demonstrated that $ZnFe_2O_4/g\text{-}C_3N_4$ with type I band alignment shows the enhanced photoinduced electrons and holes separation efficiency and enhanced photocatalytic H_2 generation activity.[47] In the case of the photocatalytic degradation of MO, we also proposed a possible mechanism based on the above results, as illustrated in Figure 10b. The MO molecules absorbed on the surface of the $CaIn_2S_4/g\text{-}C_3N_4$ photocatalyst were preferentially attacked by h^+ and then transformed to degradation products via the direct hole oxidation pathway. On the other hand, the CB electrons (e^-) accumulated on the surface of $CaIn_2S_4$ are scavenged by oxygen on the surface of the catalyst to generate superoxide radicals ($O_2^{\bullet -}$), which could also react with MO molecules.

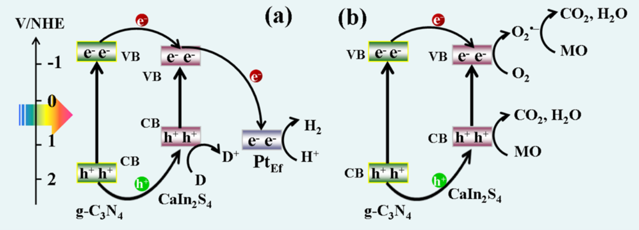

Figure 10. Schematic illustrations of the possible charge transfer for (a) H_2 production and (b) photocatalytic degradation of MO under visible light irradiation.

4. CONCLUSIONS

In summary, two-dimensional $CaIn_2S_4/g\text{-}C_3N_4$ heterojunction nanocomposites with enhanced H_2 evolution and photocatalytic degradation organic molecules activities under visible light irradiation have been demonstrated. The $CaIn_2S_4$ nanoplates anchor dispersedly across the $g\text{-}C_3N_4$ nanosheets and form a two-dimensional heterostructure with intimate interfacial contact. It was demonstrated that this two-dimensional interfacial structure could effectively improve the photocatalytic activities by promoting the charge separation. The Pt cocatalyst induced H_2 production mechanism was proposed. In addition, the results of the free radical trapping experiment and ESR analysis indicates that the photogenerated h^+ and $O_2^{\bullet -}$ are the main oxidative species for the degradation of MO. This study can provide experimental insight into design and the mechanism study of the two-dimensional heterostructure photocatalysts with enhanced photocatalytic activity.

■ ASSOCIATED CONTENT

Ⓢ Supporting Information

The Supporting Information is available free of charge on the ACS Publications website at DOI: 10.1021/acsami.5b05118.

Figures S1−S6 (PDF)

■ AUTHOR INFORMATION

Corresponding Author

*E-mail: chenmin3226@sina.com.

Author Contributions

The manuscript was written through contributions of all authors. All authors have given approval to the final version of the manuscript.

Notes

The authors declare no competing financial interest.

■ ACKNOWLEDGMENTS

This work was supported by the financial supports of National Nature Science Foundation of China (No. 21406091), Natural Science Foundation of Jiangsu Province (BK20140530), and College Natural Science Research Program of Jiangsu Province (13KJB610003).

■ REFERENCES

(1) Fujishima, A.; Honda, K. Electrochemical Photolysis of Water at a Semiconductor Electrode. *Nature* **1972**, *238*, 37−38.

(2) Murdoch, M.; Waterhouse, G. I. N.; Nadeem, M. A.; Metson, J. B.; Keane, M. A.; Howe, R. F.; Llorca, J.; Idriss, H. The Effect of Gold Loading and Particle Size on Photocatalytic Hydrogen Production from Ethanol over Au/TiO_2 Nanoparticles. *Nat. Chem.* **2011**, *3*, 489−492.

(3) Tanaka, A.; Hashimoto, K.; Kominami, H. Visible-Light-Induced Hydrogen and Oxygen Formation over Pt/Au/WO_3 Photocatalyst Utilizing Two Types of Photoabsorption Due to Surface Plasmon Resonance and Band-Gap Excitation. *J. Am. Chem. Soc.* **2014**, *136*, 586−589.

(4) Liu, B.; Liu, L. M.; Lang, X. F.; Wang, H. Y.; Lou, X. W. (David); Aydil, E. S. Doping High-Surface-Area Mesoporous TiO_2 Microspheres with Carbonate for Visible Light Hydrogen Production. *Energy Environ. Sci.* **2014**, *7*, 2592−2597.

(5) Yu, C. L.; Li, G.; Kumar, S.; Yang, K.; Jin, R. C. Phase Transformation Synthesis of Novel Ag_2O/Ag_2CO_3 Heterostructures with High Visible Light Efficiency in Photocatalytic Degradation of Pollutants. *Adv. Mater.* **2014**, *26*, 892−898.

(6) Zhang, J.; Yu, J. G.; Zhang, Y. M.; Li, Q.; Gong, J. R. Visible Light Photocatalytic H_2-Production Activity of CuS/ZnS Porous Nanosheets Based on Photoinduced Interfacial Charge Transfer. *Nano Lett.* **2011**, *11*, 4774−4779.

(7) Zuo, F.; Bozhilov, K.; Dillon, R. J.; Wang, L.; Smith, P.; Zhao, X.; Bardeen, C.; Feng, P. Y. Active Facets on Titanium(III)-Doped TiO_2: An Effective Strategy to Improve the Visible-Light Photocatalytic Activity. *Angew. Chem.* **2012**, *124*, 6327−6330.

(8) Primo, A.; Marino, T.; Corma, A.; Molinari, R.; García, H. Efficient Visible-Light Photocatalytic Water Splitting by Minute Amounts of Gold Supported on Nanoparticulate CeO_2 Obtained by a Biopolymer Templating Method. *J. Am. Chem. Soc.* **2011**, *133*, 6930−6933.

(9) Xiong, Z. G.; Zhao, X. S. Nitrogen-Doped Titanate-Anatase Core−Shell Nanobelts with Exposed {101} Anatase Facets and Enhanced Visible Light Photocatalytic Activity. *J. Am. Chem. Soc.* **2012**, *134*, 5754−5757.

(10) An, X. Q.; Yu, J. C.; Tang, J. W. Biomolecule-Assisted Fabrication of Copper Doped SnS_2 Nanosheet-Reduced Graphene Oxide Junctions with Enhanced Visible-Light Photocatalytic Activity. *J. Mater. Chem. A* **2014**, *2*, 1000−1005.

(11) Wang, X. C.; Maeda, K.; Thomas, A.; Takanabe, K.; Xin, G.; Carlsson, J. M.; Domen, K.; Antonietti, M. A Metal-Free Polymeric Photocatalyst for Hydrogen Production from Water under Visible Light. *Nat. Mater.* **2009**, *8*, 76−80.

(12) Yang, S. B.; Gong, Y. J.; Zhang, J. S.; Zhan, L.; Ma, L. L.; Fang, Z. Y.; Vajtai, R.; Wang, X. C.; Ajayan, P. M. Exfoliated Graphitic Carbon Nitride Nanosheets as Efficient Catalysts for Hydrogen Evolution Under Visible Light. *Adv. Mater.* **2013**, *25*, 2452−2456.

(13) Shiraishi, Y.; Kanazawa, S.; Sugano, Y.; Tsukamoto, D.; Sakamoto, H.; Ichikawa, S.; Hirai, T. Highly Selective Production of Hydrogen Peroxide on Graphitic Carbon Nitride (g-C_3N_4) Photocatalyst Activated by Visible Light. *ACS Catal.* **2014**, *4*, 774−780.

(14) Zhang, L.; Jing, D. W.; She, X. L.; Liu, H. W.; Yang, D. J.; Lu, Y.; Li, J.; Zheng, Z. F.; Guo, L. J. Heterojunctions in g-$C_3N_4/TiO_2(B)$ Nanofibres with Exposed (001) Plane and Enhanced Visible-Light Photoactivity. *J. Mater. Chem. A* **2014**, *2*, 2071−2078.

(15) Zhang, S. W.; Li, J. X.; Wang, X. K.; Huang, Y. S.; Zeng, M. Y.; Xu, J. Z. In Situ Ion Exchange Synthesis of Strongly Coupled Ag@AgCl/g-C_3N_4 Porous Nanosheets as Plasmonic Photocatalyst for Highly Efficient Visible-Light Photocatalysis. *ACS Appl. Mater. Interfaces* **2014**, *6*, 22116−22125.

(16) Sun, J. X.; Yuan, Y. P.; Qiu, L. G.; Jiang, X.; Xie, A. J.; Shen, Y. H.; Zhu, J. F. Fabrication of Composite Photocatalyst g-C_3N_4−ZnO and Enhancement of Photocatalytic Activity under Visible Light. *Dalton Trans.* **2012**, *41*, 6756−6763.

(17) Liao, Y. L.; Zhu, S. M.; Ma, J.; Sun, Z. H.; Yin, C.; Zhu, C. L.; Lou, X. H.; Zhang, D. Tailoring the Morphology of g-C_3N_4 by Self-Assembly towards High Photocatalytic Performance. *ChemCatChem* **2014**, *6*, 3419−3425.

(18) Liu, J.; Liu, Y.; Liu, N. Y.; Han, Y. Z.; Zhang, X.; Huang, H.; Lifshitz, Y.; Lee, S. T.; Zhong, J.; Kang, Z. H. Metal-free Efficient Photocatalyst for Stable Visible Water Splitting via A Two-Electron Pathway. *Science* **2015**, *347*, 970−974.

(19) Li, Y. B.; Zhang, H. M.; Liu, P.; Wang, D.; Li, Y.; Zhao, H. J. Cross-Linked g-C_3N_4/rGO Nanocomposites with Tunable Band Structure and Enhanced Visible Light Photocatalytic Activity. *Small* **2013**, *9*, 3336−3344.

(20) Xu, L.; Huang, W. Q.; Wang, L. L.; Tian, Z. A.; Hu, W. Y.; Ma, Y. M.; Wang, X.; Pan, A. L.; Huang, G. F. Insights into Enhanced Visible-Light Photocatalytic Hydrogen Evolution of g-C_3N_4 and Highly Reduced Graphene Oxide Composite: The Role of Oxygen. *Chem. Mater.* **2015**, *27*, 1612−1621.

(21) Xu, M.; Han, L.; Dong, S. J. Facile Fabrication of Highly Efficient g-C_3N_4/Ag_2O Heterostructured Photocatalysts with Enhanced Visible-Light Photocatalytic Activity. *ACS Appl. Mater. Interfaces* **2013**, *5*, 12533−12540.

(22) Li, Q.; Zhang, N.; Yang, Y.; Wang, G. Z.; Ng, D. H. L. High Efficiency Photocatalysis for Pollutant Degradation with MoS_2/C_3N_4 Heterostructures. *Langmuir* **2014**, *30*, 8965−8972.

(23) Li, C. J.; Wang, S. P.; Wang, T.; Wei, Y. J.; Zhang, P.; Gong, J. L. Monoclinic Porous $BiVO_4$ Networks Decorated by Discrete g-C_3N_4 Nano-Islands with Tunable Coverage for Highly Efficient Photocatalysis. *Small* **2014**, *10*, 2783−2790.

(24) Fu, J.; Chang, B. B.; Tian, Y. L.; Xi, F. N.; Dong, X. P. Novel C_3N_4-CdS Composite Photocatalysts with Organic-Inorganic Heterojunctions: in situ Synthesis, Exceptional Activity, High Stability and Photocatalytic Mechanism. *J. Mater. Chem. A* **2013**, *1*, 3083−3090.

(25) Jiang, D. L.; Chen, L. L.; Zhu, J. J.; Chen, M.; Shi, W. D.; Xie, J. M. Novel p-n Heterojunction Photocatalyst Constructed by Porous Graphite-Like C_3N_4 and Nanostructured BiOI: Facile Synthesis and Enhanced Photocatalytic Activity. *Dalton Trans.* **2013**, *42*, 15726−15734.

(26) Ding, J. J.; Yan, W. H.; Sun, S.; Bao, J.; Gao, C. Hydrothermal Synthesis of $CaIn_2S_4$-Reduced Graphene Oxide Nanocomposites with Increased Photocatalytic Performance. *ACS Appl. Mater. Interfaces* **2014**, *6*, 12877−12884.

(27) Ding, J. J.; Hong, B.; Luo, Z. L.; Sun, S.; Bao, J.; Gao, C. Mesoporous Monoclinic $CaIn_2S_4$ with Surface Nanostructure: An Efficient Photocatalyst for Hydrogen Production under Visible Light. *J. Phys. Chem. C* **2014**, *118*, 27690−27697.

(28) Liu, Q.; Lu, H.; Shi, Z. W.; Wu, F. L.; Guo, J.; Deng, K. M.; Li, L. 2D $ZnIn_2S_4$ Nanosheet/1D TiO_2 Nanorod Heterostructure Arrays for Improved Photoelectrochemical Water Splitting. *ACS Appl. Mater. Interfaces* **2014**, *6*, 17200−17207.

(29) Ye, L.; Fu, J. L.; Xu, Z.; Yuan, R. S.; Li, Z. H. Facile One-Pot Solvothermal Method to Synthesize Sheet-on-Sheet Reduced Graphene Oxide (RGO)/$ZnIn_2S_4$ Nanocomposites with Superior Photocatalytic Performance. *ACS Appl. Mater. Interfaces* **2014**, *6*, 3483−3490.

(30) Ge, L.; Han, C. C. Synthesis of MWNTs/g-C_3N_4 Composite Photocatalysts with Efficient Visible Light Photocatalytic Hydrogen Evolution Activity. *Appl. Catal., B* **2012**, *117−118*, 268−274.

(31) Wang, X. J.; Yang, W. Y.; Li, F. T.; Xue, Y. B.; Liu, R. H.; Hao, Y. J. In Situ Microwave-Assisted Synthesis of Porous N-TiO_2/g-C_3N_4 Heterojunctions with Enhanced Visible-Light Photocatalytic Properties. *Ind. Eng. Chem. Res.* **2013**, *52*, 17140−17150.

(32) Niu, P.; Liu, G.; Cheng, H. M. Visible-Light-Induced WO_3/g-C_3N_4 Composites with Enhanced Photocatalytic Activity. *J. Phys. Chem. C* **2012**, *116*, 11013−11018.

(33) Katsumata, H.; Sakai, T.; Suzuki, T.; Kaneco, S. Highly Efficient Photocatalytic Activity of g-C_3N_4/Ag_3PO_4 Hybrid Photocatalysts through Z-Scheme Photocatalytic Mechanism under Visible Light. *Ind. Eng. Chem. Res.* **2014**, *53*, 8018−8025.

(34) Chang, J. F.; Feng, L. G.; Liu, C. P.; Xing, W.; Hu, X. L. An Effective Pd-Ni_2P/C Anode Catalyst for Direct Formic Acid Fuel Cells. *Angew. Chem., Int. Ed.* **2014**, *53*, 122−126.

(35) Sun, L. M.; Qi, Y.; Jia, C. J.; Jin, Z.; Fan, W. L. Enhanced Visible-Light Photocatalytic Activity of g-C_3N_4/Zn_2GeO_4 Heterojunctions with Effective Interfaces Based on Band Match. *Nanoscale* **2014**, *6*, 2649−2659.

(36) Niu, P.; Zhang, L. L.; Liu, G.; Cheng, H. M. Graphene-Like Carbon Nitride Nanosheets for Improved Photocatalytic Activities. *Adv. Funct. Mater.* **2012**, *22*, 4763−4770.

(37) Wang, D. H.; Jia, L.; Wu, X. L.; Lu, L. Q.; Xu, A. W. One-Step Hydrothermal Synthesis of N-doped TiO_2/C Nanocomposites with High Visible Light Photocatalytic Activity. *Nanoscale* **2012**, *4*, 576−584.

(38) Shi, H. F.; Chen, G. Q.; Zhang, C. L.; Zou, Z. G. Polymeric g-C_3N_4 Coupled with $NaNbO_3$ Nanowires toward Enhanced Photocatalytic Reduction of CO_2 into Renewable Fuel. *ACS Catal.* **2014**, *4*, 3637−3643.

(39) Chen, Z. H.; Sun, P.; Fan, B.; Zhang, Z. G.; Fang, X. M. In Situ Template-Free Ion-Exchange Process to Prepare Visible-Light-Active

g-C_3N_4/NiS Hybrid Photocatalysts with Enhanced Hydrogen Evolution Activity. *J. Phys. Chem. C* **2014**, *118*, 7801−7807.

(40) Zhao, H.; Dong, Y. M.; Jiang, P. P.; Miao, H. Y.; Wang, G. L.; Zhang, J. J. In Situ Light-Assisted Preparation of MoS_2 on Graphitic C_3N_4 Nanosheet for Enhanced Photocatalytic H_2 Production from Water. *J. Mater. Chem. A* **2015**, *3*, 7375−7381.

(41) He, Y. M.; Zhang, L. H.; Teng, B. T.; Fan, M. H. New Application of Z-Scheme Ag_3PO_4/g-C_3N_4 Composite in Converting CO_2 to Fuel. *Environ. Sci. Technol.* **2015**, *49*, 649−656.

(42) Ge, L.; Zuo, F.; Liu, J. K.; Ma, Q.; Wang, C.; Sun, D. Z.; Bartels, L.; Feng, P. Y. Synthesis and Efficient Visible Light Photocatalytic Hydrogen Evolution of Polymeric g-C_3N_4 Coupled with CdS Quantum Dots. *J. Phys. Chem. C* **2012**, *116*, 13708−13714.

(43) Yu, P.; Wen, X. M.; Lee, Y. C.; Lee, W. C.; Kang, C. C.; Tang, J. Photoinduced Ultrafast Charge Separation in Plexcitonic CdSe/Au and CdSe/Pt Nanorods. *J. Phys. Chem. Lett.* **2013**, *4*, 3596−3601.

(44) Li, K.; Chai, B.; Peng, T. Y.; Mao, J.; Zan, L. Preparation of $AgIn_5S_8/TiO_2$ Heterojunction Nanocomposite and Its Enhanced Photocatalytic H_2 Production Property under Visible Light. *ACS Catal.* **2013**, *3*, 170−177.

(45) Zhang, X. H.; Peng, T. Y.; Yu, L. J.; Li, R. J.; Li, Q. Q.; Li, Z. Visible/Near-Infrared-Light-Induced H_2 Production over g-C_3N_4 Co-sensitized by Organic Dye and Zinc Phthalocyanine Derivative. *ACS Catal.* **2015**, *5*, 504−510.

(46) Jin, J.; Yu, J. G.; Liu, G.; Wong, P. K. Single Crystal CdS Nanowires with High Visible-Light Photocatalytic H_2-production Performance. *J. Mater. Chem. A* **2013**, *1*, 10927−10934.

(47) Chen, J.; Shen, S. H.; Guo, P. H.; Wu, P.; Guo, L. J. Spatial Engineering of Photo-active Sites on g-C_3N_4 for Efficient Solar Hydrogen Generation. *J. Mater. Chem. A* **2014**, *2*, 4605−4612.